




## RESEARCH ARTICLE OPEN ACCESS

# Polarons in DPP Polymers – How Glycol Side Chains and Elongated Conjugated Backbone Influence the Formation and Transport

Katherine Stewart<sup>1</sup>  | Ellasia Tan<sup>1</sup>  | Jingwan Kim<sup>2</sup> | Yun-Hi Kim<sup>2</sup> | Ji-Seon Kim<sup>1,3,4</sup> 

<sup>1</sup>Department of Physics and Centre for Processable Electronics, Imperial College London, Blackett Laboratory, London, UK | <sup>2</sup>Department of Chemistry and Research Institute of Molecular Alchemy (RIMA), Gyeongsang National University Jinju, Gyeongnam, South Korea | <sup>3</sup>Department of Chemistry, University of Oxford South Parks Road, Oxford, UK | <sup>4</sup>Department of Physics, Ewha Womans University, Seoul, Republic of Korea

**Correspondence:** Katherine Stewart ([ks2017@ic.ac.uk](mailto:ks2017@ic.ac.uk)) | Ji-Seon Kim ([ji-seon.kim@imperial.ac.uk](mailto:ji-seon.kim@imperial.ac.uk))

**Received:** 15 October 2025 | **Revised:** 28 January 2026 | **Accepted:** 6 February 2026

**Keywords:** DPP polymers | elongated conjugated backbone | glycol side chains | polarons | raman spectroscopy

## ABSTRACT

Understanding polaron formation in conjugated polymers is critical for advancing solid-state organic electronics. Here, we investigate diketopyrrolopyrrole (DPP)-based polymers with tailored side chains to elucidate the impact of glycolation on charge transport and polaron formation. We demonstrate that glycol side chains enhance p-type character and charge carrier density, while backbone elongation improves planarity and mobility. Electrochemical doping using a semicrystalline solid-state ionic liquid (SSIL) can increase conductivity by four orders of magnitude. In situ field-dependent Raman spectroscopy probes polaron formation, showing increased  $\pi$ -electron redistribution in glycolated DPP. Polaron formation of the DPPT-T conjugated backbone shows a more localised polaron with structural changes to the thiophene donor unit. Backbone elongation results in greater polaron delocalisation with lower reorganisation energy. Finally, ion-gel gated organic synaptic transistors (IGOSTs) demonstrate significant performance gains for glycolated polymers with gDPPT-T and gDPPT-TVT exhibiting strong excitatory post-synaptic currents. The more facile polaron formation pathway for gDPPT-TVT offers a significant advantage in the dynamics of ion migration and retention. This work provides molecular-level insight into the incorporation of glycol side chains to high-performance conjugated polymers for solid-state applications.

## 1 | Introduction

Oligoethylene glycol (OEG) side chains can increase the hydrophilicity, polarity, flexibility and ionic conductivity of conjugated polymers [1]. There have been significant advances in the use of  $\pi$ -conjugated polymers with glycol side chains for mixed conduction applications [2]. Polar side chains facilitate electrolyte permeation into the bulk of the active layer, thereby enhancing ionic conductivity. This modification increases the number of ion-accessible sites and promotes ion-polymer backbone interactions, which can lead to an increase in

electronic charge carrier density [3]. However, in applications such as organic electrochemical transistors (OECTs), balancing the electronic carrier mobility and the volumetric capacitance can be difficult as there is often a trade-off between ionic and electronic mobilities [4]. The glycol effect on the charge density of the conjugated backbone is often overlooked [5], and can have a significant impact on solid-state packing and energetic order/disorder on a thin film microscopic scale [6]. Glycol side chains have also been shown to increase structural disorder of conjugated polymers, which can lead to lower electronic charge mobilities [7]. Therefore, understanding the effects

This is an open access article under the terms of the [Creative Commons Attribution](https://creativecommons.org/licenses/by/4.0/) License, which permits use, distribution and reproduction in any medium, provided the original work is properly cited.

© 2026 The Author(s). *Advanced Electronic Materials* published by Wiley-VCH GmbH

of side chain functionalisation in complex environments is important for the design of high-performance devices. Glycol side chains are well-reported and investigated for use in aqueous environments, and the use of glycol side chains in solid-state applications is increasing in use, for example, to modify dielectric constants in organic photovoltaics (OPV) [6, 8]. There needs to be proper consideration of the effects of glycol side chains on electrical properties to realise and design better polymers for the future.

Ionic, electronic and balanced conduction can be improved by varying the glycol content and positioning along the side chain. Increasing the distance between the conjugated polymer backbone and the oxygen atom of the ethylene glycol unit can enable the increase of both electronic and ionic conduction [4]. Hybrid or amphipathic side chains offer an alternative strategy to achieve the benefits of glycolation without loss of electrical characteristics [9]. The addition of an amphipathic side chain with an alkylated spacer unit followed by OEG shows great promise for high electronic conduction while maintaining the benefits of glycolation. Combining the hydrophobic and hydrophilic components on the same chain enables both the enhanced solubility and processability of alkyl side chains, together with the ionic conduction provided by glycol side chains [10].

While OECTs have demonstrated excellent mixed conduction in aqueous environments, their reliance on liquid electrolytes limits stability, scalability, and integration into solid-state devices. To overcome these challenges, solid-state electronic and ionic conductors are emerging as a promising alternative, offering long-term stability and compatibility with advanced device architectures. In particular, solid-state ionic liquids (SSILs) enable electrochemical doping, allowing for controlled modulation of charge density and polaron formation. Recently, the development of SSIL with matching surface energy and stable ion diffusion has been shown to significantly improve device performance [11]. Modifying ionic liquids, for example, with alkyl chains, can increase the melting point to form a solid at room temperature and ordered mesophase structures with semicrystalline properties [12, 13]. The properties of ionic liquids are highly tunable, by varying the cation or anion, and can be favourable for thin film fabrication, including low volatility, high thermal and chemical stability, and high ionic conductivity [14]. This opens new avenues for applications such as synaptic transistors, where ion retention and dynamic charge transport are essential for emulating neuromorphic behaviour [15]. Our study addresses this gap by investigating the interplay between conjugated backbone structure, side chain polarity, and SSIL doping, providing important insights into the design of next-generation solid-state organic semiconductors.

A semicrystalline SSIL has been used to electrochemically dope conjugated organic polymers. Under electrical bias, the SSIL electrostatically interacts with the conjugated polymer backbone, resulting in a reversible increase in the conductivity without forming any permanent physical or chemical interactions. The reversibility of this interaction has been previously demonstrated using applied voltage-dependent GIXWAS and Raman spectroscopy [16]. Impedance measurements of SSIL blends have confirmed that there is no measurable ionic

mobility and therefore no ionic motion in the solid state films [17]. Blending with SSIL increases the charge density and conductivity, allowing fundamental studies of polaron formation [17].

When blending the SSIL with glycolated side chains, the interactions between the polar dipoles of the oxygen atoms in the ethylene glycol units and the charged ions must be considered. In devices, both the polymer and SSIL are in the solid state and have limited ability to move; however, prior to deposition, the polymer and SSIL components are in chloroform solution and able to entangle and aggregate together [18]. Molecular dynamic simulations of organic polymers with glycolated side chains and ions in solution showed that glycol side chains create transport pathways [19], funnelling ions toward the conjugated backbone and allowing for higher ion density around the conjugated polymer [3]. In this work, we study diketopyrrolopyrrole (DPP)-based conjugated polymers with varying side chain compositions. We compare alkylated and glycolated derivatives of DPPT-T and DPPT-TVT to understand how backbone elongation (T to TVT) and side chain polarity (alkyl to glycol) influence molecular packing, polaron formation and charge transport. Using a combination of spectroscopic, electrical, and morphological analyses, including in situ Raman spectroscopy and molecular simulations, we explore how these structural modifications affect electrical performance. Our findings provide insight into the design of conjugated polymers for solid-state applications, highlighting the effects of backbone engineering and side chain functionalisation.

## 2 | Results and Discussion

### 2.1 | Polymer Properties

Figure 1a shows the chemical structure of DPP-based polymers, and polymer properties are shown in Table S1 and detailed synthetic routes reported in literature [3]. The polymers are part of the DPP family that have been widely studied due to their high mobility and tunability [20–22]. DPPT-T is copolymerised with a shorter donor unit consisting of three thiophene rings, while DPPT-TVT extends the backbone with four thiophenes connected by a vinylene. The vinylene group introduces more flexibility to the system, which has been shown to have a planarising effect on DPP polymers [23]. The alkyl polymers (aDPP) have long branched alkyl side chains to increase solubility. We use an amphipathic side chain, formed of a C12 alkyl spacer unit followed by triethylene glycol (gDPP) to maintain a high electronic conduction while maintaining the benefits of glycolation.

#### 2.1.1 | Absorption Properties

We first investigate the changes to polymer chain order and electronic structure of the DPP polymers. The normalised thin film absorbance spectra are shown in Figure 1b. The absorbance spectra consist of a strong intramolecular charge transfer (ICT) band centred at 800 nm and a much weaker  $\pi$ - $\pi^*$  at 400 nm [24]. The  $\pi$ - $\pi^*$  of aDPPT-T peaks at 421 nm, and the elongated backbone of aDPPT-TVT redshifts the  $\pi$ - $\pi^*$  peak to 485 nm,

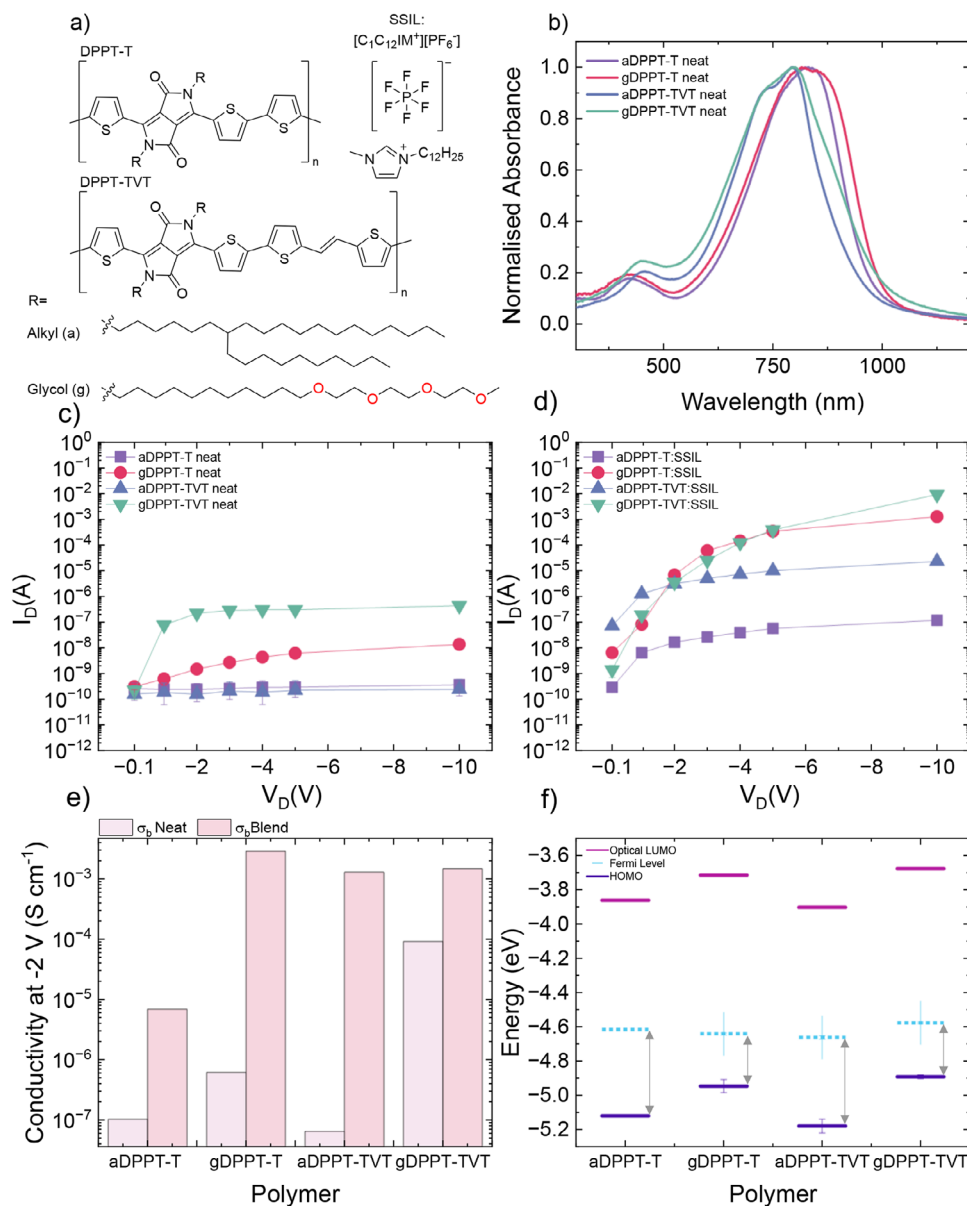


**FIGURE 1** | a) Chemical structure of DPP polymers, shorter donor unit DPPT-T and elongated backbone with vinylene unit, DPPT-TVT with branched alkyl side chains and triethylene glycol side chains with alkyl spacer, and solid state ionic liquid (SSIL)  $[C_{12}C_{12}IM^+][PF_6^-]$ , b) normalised thin film absorbance for DPP polymers. Driven voltage dependence (DVD) across  $L = 5 \mu m$   $W = 2 mm$  two-terminal device for c) neat DPP and d) blended DPP:SSIL 1:1, e) Conductivity at  $V_D = -2 V$ , comparing bulk conductivity ( $\sigma_b$ ) calculated from DVD, and f) thin film energetics, HOMO from APS and Fermi level ( $E_F$ ) from kelvin probe and LUMO extracted from optical band gap with Fermi level HOMO gap ( $E_F-HOMO$ ) shows the change in p-type character of polymers by side chain glycolation.

indicating an increased effective conjugation length. For the CT band, aDPPT-T shows a single broad peak at 830 nm, while extending the conjugated backbone to aDPPT-TVT blueshifts the  $\lambda_{max}$  to 794 nm; this blueshift suggests the overall ICT strength weakens as delocalisation over the whole backbone increases [25–27]. The aDPPT-TVT CT peak also narrows in full width half maximum (FWHM), and a shoulder peak emerges at 743 nm attributed to the 0–1 vibronic peak [28]. This vibronic shoulder suggests a greater crystallinity with better ordering and the introduction of lamella stacking in aDPPT-TVT [29]. This is due to the longer conjugation length of the extended backbone, allowing for a more rigid structure and better interdigitation of side chains due to wider spacing along the polymer chain [30].

When the side chains are glycolated, both gDPPT-T and gDPPT-TVT absorbance broadens, particularly to lower energy, most prominent in gDPPT-TVT, with the  $\lambda_{onset}$  of 1020 nm. Both the  $\lambda_{max}$  and the  $\lambda_{onset}$  red shift are indicative of increased aggregation [29].

Blending with SSIL has been shown to electrochemically dope p-type polymers. Interactions with solid-state ions create a conductivity enhancement only under the application of an applied bias, which is then reversible once the bias has been removed. As this is an electrochemical process, there is no direct chemical doping in the ground state. The first step after blending the DPP polymers at a 1:1 w/w ratio with SSIL is to confirm the

ground state interaction with absorbance spectroscopy. Evidence of chemical doping would show as a reduction in intensity of the neutral absorbance bands at 800 nm and the appearance of the polaronic band at longer wavelengths, starting >900 nm [29]. The absorbance of the DPP:SSIL blended films is shown in Figure S1a. It is clear for both alkylated and glycolated polymer blends, there is no appearance of the polaronic band beyond the neutral  $\lambda_{\text{onset}}$ . This confirms there is no permanent chemical doping interaction between DPP-based polymers and SSIL.

The absorbance spectra of the DPP:SSIL blends indicate that, even though there is no chemical doping, there is some minor morphological changes which differ between the DPP polymers arising from the entanglement and aggregation in solution [18]. For DPPT-T, the changes to the neat film order by glycolation play a prominent role in changing the blending interaction with SSIL [31]. The lower crystallinity and greater disorder in aDPPT-T lead to larger absorption changes. aDPPT-T:SSIL shows a shift to lower energy for both the  $\lambda_{\text{max}}$  and  $\lambda_{\text{onset}}$ , this is indicative of increased aggregation in the blended film. The improved polymer chain order of gDPPT-T is maintained and as such, gDPPT-T:SSIL shows no change in  $\lambda_{\text{max}}$  or FWHM, suggesting the polymer chain packing order remains largely undisturbed. There are also clear differences in film morphology observed in the AFM (Figure S2) and on a larger scale in microscope images (Figure S3), aDPPT-T:SSIL forms a mixed morphology, with some areas of isolated domains indicating poor intermixing of the polymer and ionic liquid. This is due to the poor ordering and low density of crystalline domains and suggests that SSIL does not intercalate into the crystalline domains but remains in an island-like structure and only the amorphous regions interact strongly with SSIL [32]. For the elongated backbone, the overall improved  $\pi$  stacking and interdigitation is maintained for both DPPT-TVT polymers and the absorption with SSIL decreases in FWHM, indicating greater overall packing order. aDPPT-TVT:SSIL has an increase in relative intensity of the vibronic shoulder and narrows at low energy, while for gDPPT-TVT:SSIL, there is a narrowing of both edges and a lowering of the vibronic shoulder. This change is confirmed by the AFM; there is a change from fine features to a larger interconnected network for both DPPT-TVT films, yet the topography of the blended networks has a different structure, attributed to the effect of the glycolated side chains encouraging intercalation of ions close to the conjugated backbone. The blending mechanism of SSIL into DPP polymers is dependent on neat polymer order, which is consistent with previous studies of electrochemical doping of conjugated organic polymers with SSIL, where a high crystallinity of both polymer and solid-state ionic liquid is required to enable electrochemical doping and increased electrical properties [16, 33].

### 2.1.2 | Electrical Properties and Energetics

Adding glycol side chains has been shown to increase interactions with ions and generate more electronic charge carriers in mixed conductor devices. However, the influence of glycolation on electronic-only conduction is often ignored. Here we compare the bulk conductivity in the simple two-terminal device architecture—a single-layer planar device with the DPP polymer film between gold source and drain electrodes. As a

type of conductometric sensor, the two-terminal device works as a chemiresistor to measure the resistance at a constant applied voltage with ideal behaviour showing a high and stable current at low voltage, enabling low power operation [34]. The bulk conductivity of the DPP polymers was investigated using the driven voltage dependence (DVD), a constant voltage ( $V_D$ ) applied across the source and drain electrodes and the current ( $I_D$ ) measured (Figure 1c).

Both aDPPT-T and aDPPT-TVT exhibit no current modulation with increasing voltage, this suggests limited use in chemiresistor devices, despite the high field effect mobilities achieved in field effect transistors, 0.055 and 0.102  $\text{cm}^2/\text{Vs}$  respectively (Figure S4) [3]. This low DVD highlights the importance of understanding the specifics of device applications and demonstrates that while the intrinsic mobility is high, especially in aDPPT-TVT, the number of charge carriers without a field effect is too low to achieve usable conductivity levels for chemiresistor applications. In contrast, gDPP polymers show a significant current enhancement with increasing  $V_D$ . gDPPT-T initially measures a steadily increasing current with applied voltage reaching a maximum current of 13 nA at  $-10$  V. gDPPT-TVT increases sharply with  $V_D$ , with a current of 77 nA at just  $-1$  V, this is of particular interest as increasing the current at low voltage is beneficial in creating low power devices [35]. As  $V_D$  further increases, gDPPT-TVT increases in current at a greater gradient than gDPPT-T, indicating the elongated backbone allows for faster charge transport at a lower electrical power. This agrees with field effect mobilities of gDPPT-T = 0.076  $\text{cm}^2/\text{Vs}$  and gDPPT-TVT = 0.091  $\text{cm}^2/\text{Vs}$  respectively. The bulk conductivity ( $\sigma_b$ ) is compared at  $V_D = -2$  V, to examine the conductance of charges at low voltage but above the threshold for efficient charge transport (Figure 1e). Alkylated DPP polymers have a  $\sigma_b$  in the order of  $10^{-7}$   $\text{S cm}^{-1}$  and switching to glycolated side chains increases the bulk conductivity by 1–2 orders of magnitude, demonstrating changes to electrical properties even without the introduction of mixed conduction through ions. This increase in  $\sigma_b$  suggests that glycol side chains increase the number of charge carriers even in the solid-state. The absorbance spectra indicate that there is an increase in aggregation and areas of increased packing order with the addition of glycol side chains, however, the morphological changes observed are too minor to attribute the increased conductivity to increased mobility alone.

To investigate any energetic changes associated with side chain glycolation, ambient photoemission spectroscopy (APS) and Kelvin probe were used to measure the highest occupied molecular orbital (HOMO) and Fermi levels ( $E_F$ ) for the glycolated DPP polymers (Figure 1f). The HOMO levels of the alkylated polymers are similar, aDPPT-T  $-5.12$  eV and aDPPT-TVT  $-5.18$  eV. Upon glycolation, there is a HOMO level shallowing to  $-4.95$  and  $-4.89$  eV, respectively, enabling the ease of hole injection and transport. The Fermi level of all four polymers remains nearly unchanged between  $-4.58$  and  $-4.66$  eV. This can have a strong effect on the density of states and p-type character of the glycolated DPP polymers. The optical band gap ( $E_{\text{opt}}$ ) is  $\sim 1.25$  eV for all polymers; however, the  $E_F$ -HOMO decreases from 0.5 to 0.3 eV with the addition of glycol side chains. Thus, glycol side chains seem to introduce a kind of self-doping where the Fermi level gets closer to the HOMO. This increase in p-type character can account for the increase in conductivity measured for neat gDPPT-T and gDPPT-TVT films.

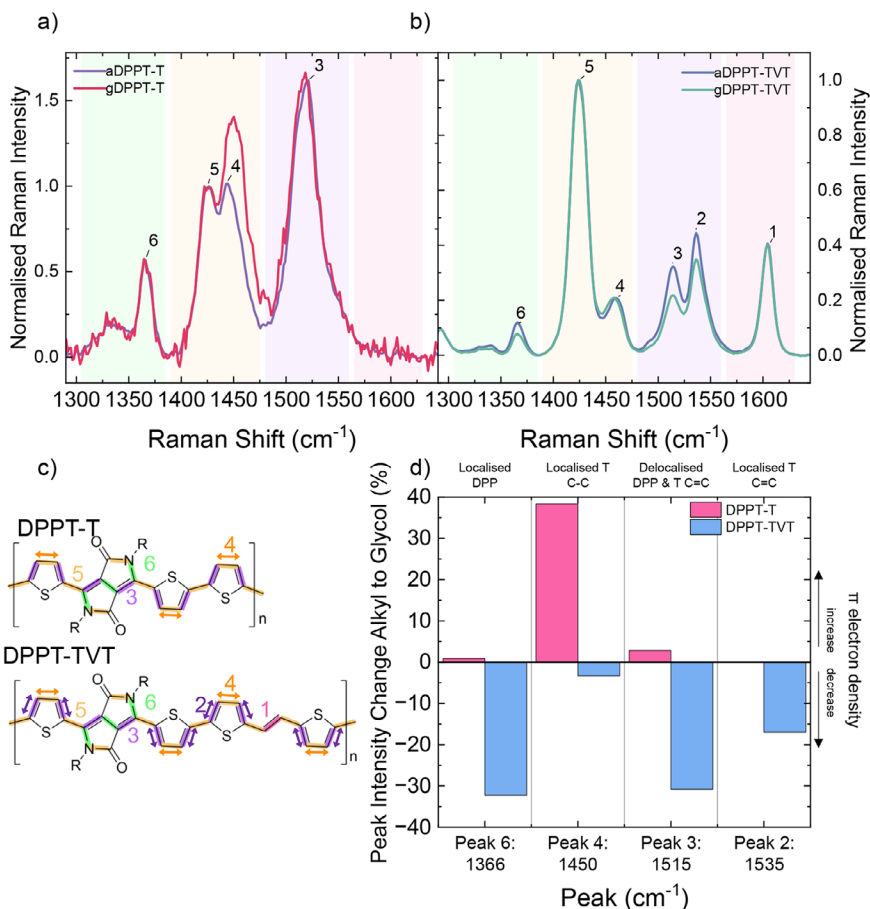


**FIGURE 2** | Normalised Raman spectroscopy at 488 nm excitation for a) DPPT-T and b) DPPT-TVt, c) structure diagram showing peak assignment with arrows indicating the more localised assignment of peaks 2 and 4, d) percentage change in relative peak intensity between alkylated and glycolated side chains.

Blending all four polymers with SSIL results in an enhancement of the current measured in the DVD (Figure 1d). Neat SSIL is insulating and does not transport charges (Figure S5) [16, 36], therefore, the strong increase in current in DPP:SSIL blends shows that there is a beneficial interaction between SSIL and the polymer conjugated backbone. aDPPT-T:SSIL has a small increase in current of nearly two orders of magnitude, showing current modulation by increased applied voltage. aDPPT-TVt:SSIL is significantly enhanced, reaching currents of 3  $\mu\text{A}$  and a  $\sigma_b$  increase of >4 orders of magnitude at  $V_D = -2$  V. This indicates aDPPT-TVt's highly ordered polymer chain packing enables strong and favourable interactions with the SSIL to increase charge carrier density and therefore conductivity. When the glycolated polymers are blended with SSIL, the  $\sigma_b$  exceeds that of the equivalent alkyl side chains and currents >1 mA at  $V_D = -10$  V were measured for both gDPPT-T and gDPPT-TVt, indicating a favourable interaction between the polymers with glycol side chains and the SSIL. This is in part due to the shallowing of the HOMO level, which can enable increased charge injection from the gold electrodes and increase the charge density. Blending with SSIL has a stronger impact on gDPPT-T than gDPPT-TVt in terms of current; the increase from neat to blend is four orders of magnitude for gDPPT-T compared to three orders of magnitude for gDPPT-TVt. Additionally, the absolute currents measured are higher for gDPPT-T:SSIL at low voltage, resulting in the highest  $\sigma_b$  of 2.9

$\times 10^{-3} \text{ S cm}^{-1}$  at  $V_D = -2$  V. We used the field effect properties to calculate an estimate of charge carrier density from the field effect conductivity ( $\sigma_E$ ) and saturated mobility (Figure S6) [37]. This demonstrates that despite the lower mobility, gDPPT-T measures the highest  $\sigma_E$ , also indicating a higher charge carrier density.

Electrical characterisation of the DPP polymers has shown the importance of elongating the conjugated backbone to increase the mobility, however the most critical step in increasing conductivity is the increase in charge carrier density enabled by glycol side chains. This is achieved by adding glycol side chains and blending with SSIL. Our results demonstrate that glycolating DPPT-TVt has a stronger effect on increasing conductivity, while blending gDPPT-T with ionic liquid has greater enhancement, leading to an overall higher performance. We show that changing the thin film morphology from ordered, closely packed domains to a less ordered but more interconnected network of polymer chains in close proximity to the ions of the SSIL, helps to increase polaron generation and therefore conductivity. For electrochemical doping with SSIL, the high blending ratio has been shown to be beneficial; in this work, a 1:1 blending ratio was used, resulting in an SSIL density of approximately three anion per monomeric unit. Previous results have shown that very high blending concentrations of up to 1:10 DPPT-T:SSIL continue to enhance conductivity [36]. This is a particularly high doping ratio

in comparison to chemical doping levels of fractions of a per cent of the host polymer [38]. This displays a significant difference to the effect of crystallinity on chemical doping, which has been shown to be highly dependent on doping ratio, with a high doping ratio resulting in disorder and poor conductivity enhancement [39].

### 2.1.3 | Raman Spectroscopy

Elongating the conjugated backbone and adding glycolated side chains has enhanced the electrical performance through increased mobility and increased charge density, respectively. To understand the origin of these changes, Raman spectroscopy was used to probe the electron-phonon coupling and investigate molecular conformational change across DPP modification and blending [29]. Raman spectroscopy is a versatile technique that can be used to examine the effect of changes to the chemical environment down to the individual bond vibrations. Raman spectra give information about vibrational modes, which can then be used to understand molecular conformation and morphology [40].

The main conjugated backbone peaks for DPPT-T and DPPT-TVT polymers are shown in Figure 2a and b, respectively. Raman excitation at 488 nm is in resonance with the  $\pi$ - $\pi^*$  absorption band, while excitation at 785 nm is in resonance with the CT absorption band, this shows fewer peaks with less variation in Raman signature between the polymers, Figure S7. The peaks are assigned by DFT, and with reference to literature [3, 16, 29], a summary of the peak assignment is shown in Figure 2c and in detail in Figure S8. DPPT-T and DPPT-TVT share many of the same Raman peak assignments; however, extending the backbone has a few noticeable changes. Most prominently there is the introduction of the vinylene (V) C=C stretch at  $1604\text{ cm}^{-1}$  (Peak 1), the splitting of the DPP and thiophene (T) C=C peak from one broad peak at  $1520\text{ cm}^{-1}$  (3) with small shoulder to two distinct peaks at  $1514\text{ cm}^{-1}$  (3) and  $1536\text{ cm}^{-1}$  (2). This peak splitting suggests the elongated backbone has more distinct differences in the environment of the thiophene ring double bonds. There is also a significant difference in the relative peak intensities, with a much greater peak intensity on the delocalised C—C stretch (5) across the backbone, indicating a greater degree of delocalisation present along the elongated TVT backbone. This correlates well with the DFT simulations showing a greater planarity in DPPT-TVT oligomers, where the mean dihedral angle is  $2.67^\circ$  for DPPT-T and  $1.44^\circ$  for DPPT-TVT.

When the alkyl side chains are switched for glycols, there are noticeable changes to the steady state Raman (Figure 2d). In the case of gDPPT-T, there is a significant relative intensity increase of the C—C<sub>intra</sub> localised thiophene peak (4) with respect to the more delocalised C—C vibration (5) across the whole backbone. This shows the glycol side chains increase the resonance of the donor thiophene unit, indicating a greater distribution of  $\pi$ -electron density on the donor unit. For gDPPT-TVT, upon glycolation, there is a relative intensity reduction of the C = C peaks, stronger for the more delocalised C=C mode (3), which includes the DPP unit and correlates with the percentage reduction of the DPP mode (6). This indicates a differentiation between the peaks with stronger DPP resonance decreasing relative to the

peaks resonant with the thiophene donor unit, suggesting a redistribution of  $\pi$ -electron density to the donor unit in the ground state. Glycolation of the two polymers has different effects on relative Raman intensity; gDPPT-T has an increase in peak intensity relative to the whole backbone, indicating less  $\pi$ -electron delocalisation, whereas gDPPT-TVT measures a decrease in relative intensity, suggesting greater delocalisation. This links to the change in packing conformation induced by the change of the side chain. The transition from bimodal ‘face-on’ dominant orientation to more ordered ‘edge-on’ in gDPPT-T can lead to increased close packing, resulting in increased intramolecular rigidity, increasing the localisation along the backbone [3]. In contrast, DPPT-TVT shows minor molecular packing changes from alkylated to glycolated, with a slightly increased  $\pi$  spacing for gDPPT-TVT, allowing for increased planarity and delocalisation.

Raman spectroscopy is used to confirm the effects of blending the conjugated polymer with SSIL. SSIL does not absorb in the visible spectrum and has no Raman active modes, so it does not introduce any new Raman peaks. Any changes to the Raman spectra are hence due to changes to the polymer conformation upon SSIL blending, not the ionic liquid itself. In DPP:SSIL, the majority of Raman features are maintained for all four DPP polymers, confirming the conjugated backbone conformation is largely unaffected in the ground state, Figure S1b. There are some very small changes in relative intensity occurring around the C=C (DPPT-T 3 and DPPT-TVT 2) and C—C (4) modes relating to the thiophene rings. This suggests SSIL interaction with the conjugated backbone is focused around the thiophene units, in agreement with the interaction of SSIL occurring preferentially with the donor unit [16].

## 2.2 | Probing Polaron Formation

### 2.2.1 | Electric Field Dependent Raman Spectroscopy

To understand the polymer structure dependence on polaron formation, we employed in situ monitoring using electric field-dependent Raman spectroscopy (EFDRS). EFDRS utilises electrochemical doping to induce a high density of polarons within the polymer thin film and allows monitoring of polaron formation. We correlate the experimental results with geometry simulations of simplified single strands in the gas state.

When a conjugated polymer is charged, a polaron forms, resulting in a lattice distortion and structural change. The structural change includes a redistribution of  $\pi$ -electron density, which can be visualised as a change in relative peak intensity and a change in bond length, shown by a change in peak position in Raman spectra. While it is sometimes possible to probe the polaron formation in OFET devices, the density of polaronic species is incredibly low and difficult to monitor. This is because only the first few monolayers in the active layer form the charge transport channel in an OFET [41]. The field effect tends to be confined to the interfacial region between the semiconducting channel and the dielectric layer and can be thought of as 2D [42]. Therefore, bulk conductance methods of examining polaron formation tend to be required.

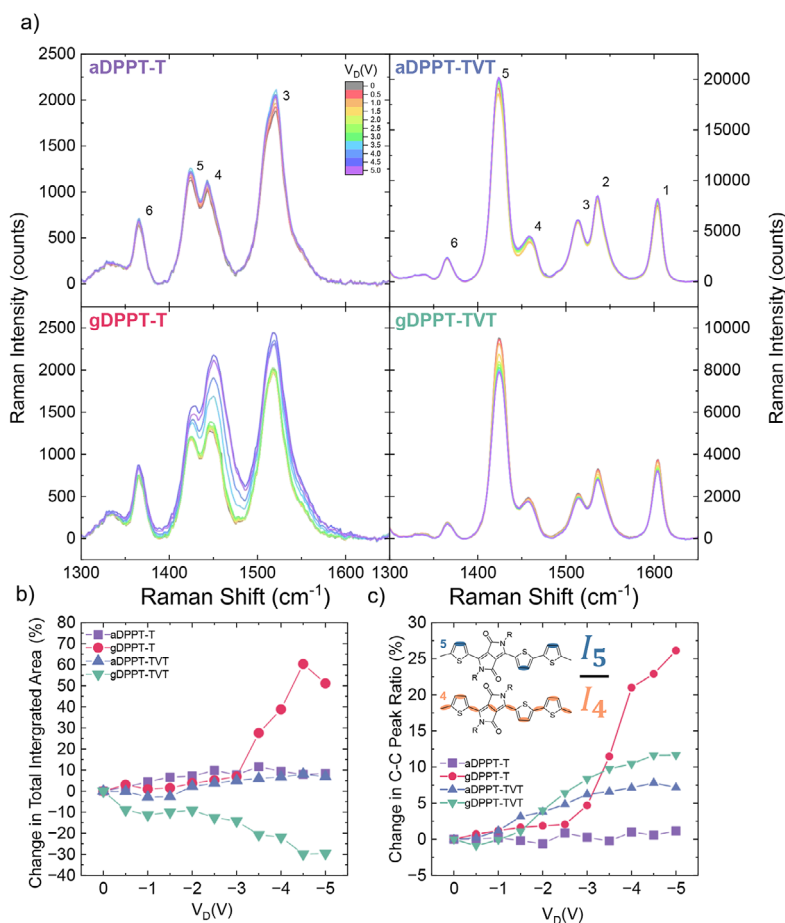


**FIGURE 3** | a) In situ electric field-dependent Raman spectroscopy (EFDRS) with 488 nm excitation for DPP:SSIL polymers under applied bias b) change in total integrated Raman area showing the change from  $V_D = 0$  V and c) change in C–C peak ratio  $I_4/I_5$  showing the relative change of  $\pi$ -electron distribution between the whole backbone and thiophene donor unit.

Spectroelectroabsorbance was used to understand the changes in resonant Raman spectroscopy observed as charges are formed and the lattice distortion affects the energetic transitions of the polymer. In all DPP polymers, there is a strong quenching of the main absorbance band at 800 nm, Figure S9. However, at 488 nm, the low energy onset of the  $\pi$ - $\pi^*$  absorbance band, there are changes between the two conjugated backbones: for DPPT-TVT, the  $\pi$ - $\pi^*$  quenches, but for DPPT-T, there is a quenching and broadening, resulting in an increase in absorbance at 488 nm, Figure S9c. This change in absorbance spectra with applied voltage indicates a rearrangement of molecular orbitals, shifting the energetics of optical transitions in the DPPT-T polymers as charges are formed.

The EFDRS of the four DPP blends is measured under a 488 nm Raman probe. This excitation is in resonance with the edge of the  $\pi$ - $\pi^*$  absorbance band and provides detailed in situ characterisation of the  $\pi$  conjugated backbone under polaron formation. A source drain bias is applied across a 5  $\mu\text{m}$  channel varying from 0 to  $-5$  V. Figure 3a shows the Raman spectra averaged along the chemiresistor channel at each applied voltage. The normalised spectra and neat films are shown in Figures S10 and S11. The change in total integrated area (Figure 3b) is used to quantify the strength of the Raman signal and the changes in resonance at 488 nm excitation over the applied bias range.

Here, the change in Raman peak area is an estimation of the change in Raman cross section and indicates an increase or decrease in the overall concentration of resonant molecules. This is highly linked to the absorbance at the excitation wavelength. When probing the neutral band under bias, it is expected that the neutral resonant Raman intensity will decrease in line with the respective absorbance band decreasing. The change in resonance is small for the alkylated DPP polymers. Coupled with the low current measured for aDPPT-T (Figure 1d), this suggests poor interaction with ions in the SSIL and low polaron formation. When glycolated, there is an increase in resonance for gDPPT-T and a decrease for gDPPT-TVT, following the change in absolute spectroelectroabsorbance (Figure S9c). This further suggests the critical role glycolated side chains perform in ensuring strong ion-polymer interaction even in the solid state.

The change in relative peak intensity and shifts in peak position can be used to probe changes to the backbone conformation and molecular structure as polarons form on the polymer chain. Figure 3c shows the relative peak intensity ratio between the two C–C peaks, ( $I_4/I_5$ ), which shows the change in  $\pi$ -electron distribution between the backbone as a whole and concentrated to the thiophene donor unit. aDPPT-T shows no change in peak position and relative intensity as the drain voltage increases. This

indicates there is little conformational change induced, indicating there is no measurable lattice distortion to stabilise charge. This suggests there is a higher energy barrier to stabilise and transport charges, which correlates with the four orders of magnitude lower in situ current measured (Figure S11b) and the reduced current and conductivity shown in Figure 1. The other three DPP polymers show a relative increase in the C–C thiophene mode, confirming an increase in concentration of  $\pi$ -electrons around the donor unit as hole polarons form. This increase is strongest in gDPPT-T, where there is an increase in spectroelectroabsorbance (Figure S9c) and an increase in overall Raman signal (Figure 3b).

The degree of change measured in EFDRS can be explained with reference to density functional theory (DFT) simulations of hole polaron formation on isolated DPP trimers in the gas state. Reorganisation energy (RE) is the energy required to stabilise a charge during polaron formation, due to the strong phonon-electron coupling and lattice distortion; energy is required to redistribute the charge [43]. Figure S12a shows a larger simulated inner RE for aDPPT-T (0.143 eV) and gDPPT-T (0.146 eV) than for the elongated backbone DPPT-TVT (<0.1 eV). This confirms the change in EFDRS, where a greater degree of structural change is expected for DPPT-T as a larger lattice distortion is required to stabilise the charge. In gDPPT-T, the larger simulated RE correlates with the high reorganisation of  $\pi$ -electron density shown in the experimental in situ Raman. While aDPPT-T shows that the higher simulated reorganisation energy coupled with the low polymer-ion interaction creates a limiting step, preventing polaron formation and resulting in a low current and no experimental Raman signatures measured.

Furthermore, gDPPT-T EFDRS also shows other significant peak-to-peak changes upon polaron formation. As well as the significant increase in C–C ratio (Figure 3c), there is simultaneously shifting of the peak centre by  $3\text{ cm}^{-1}$  and an increase of the FWHM, indicating a stronger  $\pi$ -electron density and a greater distribution of energetic states. The peak shift rises sharply at  $V_D = -3\text{ V}$ , in conjunction with the current increasing from 0.2 to 1.5  $\mu\text{A}$  (Figure S11b). This increase in peak position signifies the C–C bonds of the thiophene units shortening with increased voltage, indicating a shift to more double-bond-like character. Additionally, the relative peak intensity of the DPP mode (6) and the DPP and thiophene C=C mode (3) decreases with respect to the delocalised backbone mode (5), indicating a reduction in  $\pi$ -electron density about these bonds. Thus, the EFDRS shows a  $\pi$ -electron decrease over the DPP unit.

The impact of stabilising the charge is confirmed in simulation by investigating the bond length alternation (BLA), the average difference between the length of the C–C and C=C [44] which can be used to assess the benzoidal or quinoidal behaviour of a conjugated backbone, Figure S12b. Overall, DPPT-T has a larger change in BLA ( $\Delta\text{BLA}$ ), showing that the change in structure required to accommodate the charge is higher. The major change comes from the polaronic geometry optimisation, which shows that there is a significantly lower BLA for charged DPPT-T compared to charged DPPT-TVT. This means that the energetic cost to stabilise the charge has greater impact across the

bonds of DPPT-T, while the charge is stabilised over the extended conjugated backbone with lower disruption to the benzoidal character for DPPT-TVT.

When the backbone donor unit is elongated to DPPT-TVT, the in situ current is increased, confirming the higher charge mobility and conductivity. The EFDRS of aDPPT-TVT shows minimal peak changes, with no changes in peak position or peak width. There is a relative peak intensity increase for the C–C peak ratio (Figure 3c) concurrent with a decrease in both C=C modes. Indicating a shift from a highly benzoidal structure toward a more equal distribution of  $\pi$ -electron density as polarons form along the highly planar backbone. As with aDPPT-TVT, there is no significant deviation of peak position or width in gDPPT-TVT. gDPPT-TVT EFDRS quenches as  $V_D$  is increased (Figure 3b), in agreement with the decrease in absorbance measured in the electrochemical cell (Figure S9c). In addition to showing a strong quenching under increased bias, gDPPT-TVT also demonstrates a selective quenching of the delocalised C–C mode (5), resulting in a relative increase of all other peaks. The ratio of the localised thiophene C–C (4) (Figure 3c) to the delocalised C–C increases while the overall Raman signal decreases (Figure 3a,b). This indicates that while the neutral resonance is decreasing, there is a concentration of  $\pi$ -electron density around the thiophene donor unit.

DFT simulations of individual bond lengths (Figure S12c) show that bond length changes across DPPT-T and DPPT-TVT are similar, but with a slightly lower magnitude of bond length change across all bond types for DPPT-TVT. This indicates that it is not the inclusion of one particular unit that decreases the required lattice distortion, but a greater stabilisation across the whole backbone due to the longer conjugation length. Another factor in charge delocalisation is the planarity of the conjugated backbone; planarising or locking units can significantly increase charge delocalisation [45]. Simulation of the dihedral angles along a trimer confirms that DPPT-TVT is significantly more planar, with the highest torsion angle between adjoining thiophene units measuring only  $2.8^\circ$ , compared to  $5.8^\circ$  in DPPT-T. When a charge is added, there is rearrangement and delocalisation along the backbone, which leads to a change in the dihedral angles (Figure S12d), this can account for a significant proportion of the reorganisation energy required. Dihedral angle simulations show that the more planar DPPT-TVT requires less change to the dihedral angle as a charge is added, contributing to a lower RE.

The peak signatures upon polaron formation for the DPPT-T polymers show a number of key differences to DPPT-TVT. DPPT-T polaron formation is more localised, with greater lattice distortion and a higher reorganisation energy, which limits polaron formation, so that aDPPT-T is unable to overcome the energetic barrier and measures low currents. The shallowing of the HOMO and increase of long-range order in gDPPT-T enable polaron formation and can be probed by EFDRS to identify the localisation of  $\pi$ -electron density and bond length changes to the thiophene donor unit. EFDRS shows the transition from isolated localised polarons in DPPT-T to the delocalised extended polaron wavefunction of DPPT-TVT. Both aDPPT-TVT and gDPPT-TVT show small peak signature shifts and measure high currents, indicating a greater distribution of the lattice distortion across the backbone.

## 2.2.2 | Synaptic Ion Interactions

To examine the change in polaron formation and retention, the DPP polymers were tested in ion-gel gated organic synaptic transistors (IGOSTs). Organic synaptic transistors (OST) emulate the pulse and memory effect of biological synapses, where the synaptic electrical spike is passed from the gate electrode through a solid-state ionic gel layer [46]. This causes the migration of ions into the organic semiconductor layer and induces a postsynaptic response. OSTs share similarities with blending with SSIL due to the solid-state nature of the device but also with OEETs, where ion penetration plays an important role. DPP-based OSTs have proven to be difficult to electrochemically dope and result in short retention times, however recent research has used molecular engineering to improve synaptic retention. Current amplitudes and retention times have been improved by including an alkyl spacer between the backbone and the branched side chain [47], adding glycolated side chains [48], and blending alkylated and glycolated polymers [49]. The DPP polymers in this work have a C6 and C12 spacer for alkylated and glycolated side chains and show a variety of polymer chain order properties depending on the conjugated backbone and side chain combination. Solid-state chemiresistor measurements and in situ Raman spectroscopy have shown that the electrical properties can be tuned by interaction with ions. We demonstrate how understanding of polaron formation can explain changes in IGOST.

The IGOST transfer curves (Figure S 13a) show classic hysteresis behaviour, confirming the ion doping and dedoping process through the ion gel. We used a single gate pulse to compare the interaction of dynamic ionic behaviour to our results from static SSIL blends. A single pulse was chosen in order to probe ion infiltration and back diffusion processes, which enables comparison with the molecular structural change required for the transition from neutral to polaronic. The application of a single gate pulse works to push ions from the ion gel into the active polymer layer, resulting in an increase in the drain current. Figure 4a shows a representative of the drain current measured for each polymer at  $V_G = -3$  V with a 2 s pulse duration. The OFF current is similar for the four transistors, below  $10^{-7}$  A. Upon the application of the gate pulse, there is no change in current for aDPPT-TVT and a small current increase for aDPPT-T, which immediately drops once the synaptic pulse is complete. Hence, neither alkylated DPP polymers show synaptic behaviour under these conditions. In contrast, gDPPT-T and gDPPT-TVT increase dramatically in current and then show a retention of the current enhancement long after the synaptic pulse. This shows there is significant ion retention and memory effect for the glycolated polymers.

To understand how the change to backbone and side chains affects the interaction of ions and, therefore, polaron formation, the maximum excitatory postsynaptic current (EPSC) can be used to quantify the current induced under a short synaptic pulse. Figure 4b shows the maximum EPSC as a function of pulse amplitude to quantify the spiking voltage-dependent plasticity (SVDP). Spiking time-dependent plasticity (STDP) is shown in Figure S13b. Alkylated DPP show no increase in current with pulse amplitude, indicating the penetration of ions into the material from the ion gel is low and does not induce a beneficial interaction with the conjugated backbone. This differs from blending aDPPT

with SSIL in solution, where there is an opportunity in solution for the intercalation of ions into the polymer chain packing, allowing for current enhancement under sustained drain voltage application. This indicates that ions cannot easily migrate into the alkylated polymer domains and the low EPSC correlates with the lack of current enhancement measured in neat chemiresistor DVD (Figure 1c). In contrast to SSIL electrical characterisation shown in Figure 1d, IGOST aDPPT-T performs slightly better than aDPPT-TVT, showing a small EPSC increase at  $V_G = -3$  V and greater. This is likely due to the changes in crystallinity of the neat film, whereby aDPPT-T is more disordered and 'face-on' in orientation [3] allowing more amorphous domains and boundaries for polymer-ion interaction. Instead, glycolation of the side chains has a much stronger, highly beneficial effect on the synaptic behaviour, demonstrating the benefits for ion permeation. The maximum EPSC for gDPPT-T increases from  $V_G = -3$  V, reaching 0.9 mA. gDPPT-TVT increases from a lower pulse amplitude and saturates at  $-3.5$  V with a maximum EPSC of 4 mA. Comparing the IGOST current with DVD current, EPSC shows a three order of magnitude increase on application of a 2 s  $-3$  V pulse, comparable to the four order of magnitude increase for  $-3$  V in DPP:SSIL blends (Figure 1d) and far exceeds the current enhancement of the neat DPP DVD (Figure 1c). Thus, ion migration into the gDPPT-T and gDPPT-TVT films is shown to be fast and efficient.

The retention of ions is important for the memory behaviour of synaptic devices. The memory retention (R) is measured as the percentage of the maximum EPSC induced (Figure S13c). In this work, the single  $V_G$  pulse induces a low but measurable increase in EPSC over 60 s after the synaptic pulse in both gDPPT-T and gDPPT-TVT. The retention is higher for gDPPT-TVT  $V_G = -3.5$  V, showing an  $R_{60}$  of 3.5%, compared to just 0.7% for gDPPT-T. This suggests the retention of ions is enhanced by the higher crystallinity of the elongated backbone, whereby ions penetrate and form interactions with more highly ordered conjugated backbones. The lower reorganisation energy and higher mobility of gDPPT-TVT enable increased ion interaction and reduced ion back diffusion [50].

The shape of the EPSC during the  $V_G$  pulse shows the changes in ion permeation. Figure 4c shows the normalised EPSC over the duration of the gate pulse as the  $V_G$  is increased. gDPPT-T shows a constant current increase rate with a high linearity with a 10–90% rise time of 1.38 s for  $V_G = -3.0$  and  $-3.5$  V. The turn on indicates a steady rate of ion migration into the polymer layer, resulting in an increase in EPSC over the pulse period. For gDPPT-TVT, the turn on dynamics increase over the range of voltage applied, starting at 1.59 s at  $V_G = -2.0$  V and decreasing to 1.37 s for  $V_G = -3.0$  V. There is a dramatic shift at  $V_G = -3.5$  V, where the turn on is nonlinear, with a rise time of only 0.68 s, twice as fast as gDPPT-T under the same conditions. The increasing EPSC rate indicates a change in ion migration, whereby a threshold voltage has been overcome to induce a higher density of ion infiltration and interaction with the gDPPT-TVT backbone. It is likely this onset for gDPPT-TVT is linked to the lower reorganisation energy (Figure S12a) and decreased molecular structural change required to induce polaron formation (Figure 3c) than for gDPPT-T.

IGOST measurements rely on dynamic ions moving in and out of the conjugated polymer under the influence of synaptic pulses.

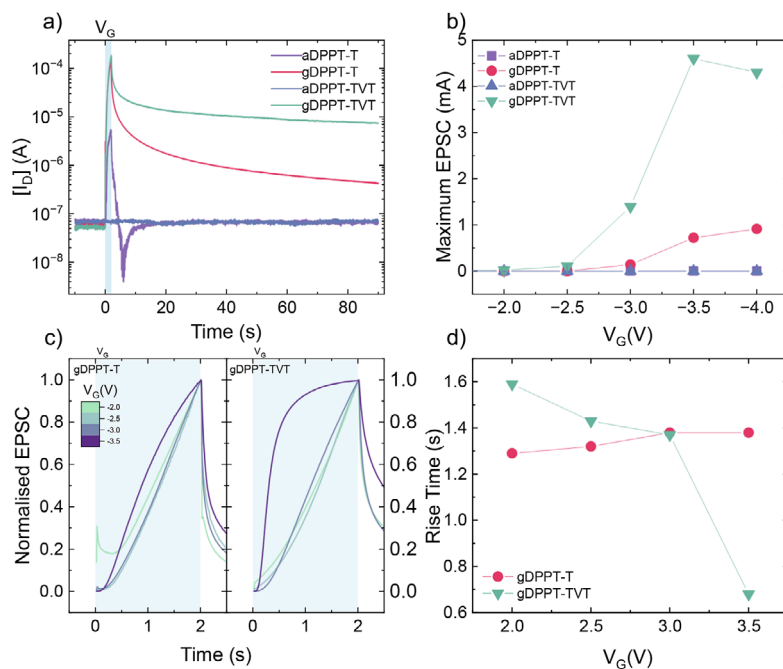


**FIGURE 4** | IGOST Device Characteristics a) Synaptic pulse measurement showing the application of a -3 V gate pulse for 2 s, b) Spike voltage dependent plasticity (SVDP), the maximum excitatory postsynaptic current (EPSC) measured as a function of pulse amplitude, c) EPSC for SVDP normalised over pulse duration for gDPPT-T and gDPPT-TVT and d) rise time for SVDP from 10% to 90% of pulse height.

This differs highly from the static blended properties of SSIL blends, where anions must intercalate with conjugated polymers in solution before being cast. In SSIL blends, the neat polymer order is disrupted by the active anions and the bulky cations as they are blended to form an interconnected network [33]. A balance of high crystallinity and flexibility to accommodate ions is required to electrochemically dope the polymer and enhance conductivity. In this work, we have shown that the impact of glycolation on packing order and shallowing the HOMO level allows for greater electrochemical enhancement of gDPP polymers, with the magnitude of enhancement being greater for gDPPT-T. In synaptic measurements, the DPP polymer order is of the neat film packing and ions must infiltrate into the bulk, sharing many dynamics of OECTs without the swelling by the electrolyte. Our results show a significant increase in EPSC induced for gDPPT-TVT over gDPPT-T, this is likely to be due to the increased polymer order, longer backbone length and greater spacing between side chains. The combination of glycol side chains to encourage ion distribution close to the backbone and the strong ion-polymer interaction with the extended planar donor unit works to increase the rate of ion migration during the synaptic pulse, increasing the rise time and the maximum EPSC. After the synaptic pulse, the higher ion retention in gDPPT-TVT is linked to a higher density of ions with strong ion-polymer interactions due to lower reorganisation energy and the capability to form and delocalise more polarons.

### 3 | Conclusion

In this work, we have investigated the molecular structure-property relationship of DPP polymers to understand the effect of backbone elongation and side chain substitution on polaron formation and charge transport. We demonstrate that backbone

elongation reduces molecular structural change upon polaron formation through increased planarity and greater delocalisation, thus increasing the charge transport and conductivity. Glycolation can have a profound effect on polymer properties, especially in the case of lower mobility, higher disorder DPPT-T. Adding glycol side chains increases the p-type character of the DPP polymers, increasing conductivity and reducing the barrier to lattice distortion.

The conductivity of the DPP polymers can be improved by electrochemical doping with SSIL. Solid-state electrochemical doping could be used to overcome difficulties in achieving high charge carrier densities with commercially available molecular dopants due to the deep HOMO of DPP polymers. We show that the SSIL interaction is stronger for glycolated DPP polymers and enables a high density of polarons. Using EFDRS as an in situ Raman probe, we are able to determine the difference in polaron formation mechanism and confirm with simulation. DPPT-T has a larger molecular structural change, creating more localised polarons concentrated over the thiophene donor unit. DPPT-TVT enables more polaron delocalisation, decreasing the molecular structural change required. In IGOSTs, the lower energy lattice distortion and greater delocalisation of polarons of gDPPT-TVT allow for faster polaron formation and longer ion retention.

## 4 | Experimental Section/Methods

### 4.1 | Materials

DPP-based polymers were synthesised by Y.H. Kim group and summarised in Table S1 [3]. Solid state ionic liquid 1-dodecane-3-methylimidazolium hexafluorophosphate ( $[C_{12}IM^+][PF_6^-]$ ),

was synthesised through a conventional method described elsewhere [36].

## 4.2 | Film Preparation

DPP neat and blended with SSIL were dissolved in chloroform at a  $5 \text{ mg/mL}^{-1}$  and stirred at  $40^\circ\text{C}$ , before being spin coated on to cleaned substrates at 2000 rpm/40 s. Chemiresistor and bottom-gate bottom contact OFET devices were fabricated using Fraunhofer silicon wafers with a silicon dioxide layer, and the source and drain electrodes ( $W = 2 \text{ mm}$   $L = 5 \mu\text{m}$ ) formed of a 10 nm ITO adhesion layer and topped with 30 nm of gold and thin films were spun on quartz, ITO and FTO substrates under the same conditions. Films were dried in a desiccator overnight and stored in  $\text{N}_2$ .

## 4.3 | Absorbance and Energetics

The absorption of thin films on quartz was measured Shimadzu UV-2600 UV/visible spectrophotometer with an integrating sphere attachment. Air was used as a baseline reference, and the thin film samples were corrected to the transmission of a clean blank quartz substrate. Spectroelectrochemical absorbance measurements were measured of neat DPP polymers on FTO-coated glass substrates. A custom electrochemical cell was used with Pt counter electrode, Ag/AgCl reference electrode and acetonitrile electrolyte (0.1 M TBAPF<sub>6</sub>). Oxidising potential was applied using an Autolab potentiostat PGSTAT101, and transmission spectra were collected in reference to a blank FTO substrate in the electrochemical cell. The HOMO energy level of the neat films was measured by Ambient Photoemission Spectroscopy (APS) with an APS04 from KP Technology. The Au tip was calibrated by calculating the absolute tip work function with respect to the vacuum using an Ag reference sample. Thin films were spun onto cleaned ITO substrates and kept in the dark in  $\text{N}_2$  prior to measurement. The cube root of the photoemission signal was linearly fitted to calculate the HOMO of the sample, and the mean of three measurements was taken. The LUMO was estimated from the optical energy gap, the onset of absorbance, and the HOMO level by APS.

## 4.4 | Electrical Characterisation

Chemiresistor performance was measured using Driven Voltage Dependence (DVD) measurement on a probe station in a nitrogen glovebox. A drain voltage is held between the source and drain electrode for 10 s, and the drain current is measured. The mean current for each applied voltage is extracted to evaluate the device performance, and bulk conductivity ( $\sigma_b$ ) is calculated from the current, taking into account the channel dimensions. OFET transfer and output curves were measured,  $V_D = -10$  and  $-60 \text{ V}$  and  $V_G$  sweep =  $+20$  to  $-60 \text{ V}$  and field effect conductivities extracted using the transfer line method [51]. IGOST measurements were carried out using the same device architecture as a chemiresistor with the application of an ion gel, drop cast from 1:4:11 [EMIM][TFSI]:PVDF-HFP:acetone with a micro-positioner probe as the gate electrode. OST transfer sweeps were measured at  $V_D = -0.5$  and  $-1 \text{ V}$  with  $V_G$  sweeps from  $+3.5$

to  $-3.5 \text{ V}$ , synaptic pulse measurements were taken with a single pulse of duration 0.5 to 2 s at  $V_D = -1 \text{ V}$  and varying  $V_G$  from  $-0.5$  to  $-4.0 \text{ V}$ .

## 4.5 | DFT Simulation

Raman peak assignment and geometry analysis were simulated using density functional theory (DFT) on the Imperial College High-Performance Computing service using GAUSSAIN09 software [52]. All simulations were performed on single molecules in the gas phase using the B3LYP level of theory and basis set 6-31G(d,p) [53–55]. DPP polymers were simulated for with donor unit end groups for dimers (D-A-D-A-D) and trimers (D-A-D-A-D-A-D) with hexyl side chains ( $-\text{C}_6\text{H}_{13}$ ) for alkyl DPP and methoxybutane ( $-(\text{CH}_2)_4\text{OCH}_3$ ) to simulate glycol. The frequency of vibrations was identified from simulations of Raman spectra using an empirical scaling factor of 0.97 [56], and peak assignments were visualised using GaussView 6.0.16 software [57]. Geometry data and Hirshfeld charges were extracted from the optimisation calculations, and the reorganisation energy was calculated. Simulated neutral and polaronic states give the final optimised geometry for the oligomer in the gas state, allowing detailed comparison of the observed experimental changes with the changes to individual bonds from the neutral state to their final state under a stable, fully delocalised charge.

## 4.6 | Atomic Force Microscope

Thin film topography was measured on a Park NX10 AFM system using true non-contact mode with an NCM-NHCR tip. AFM Z height images were processed and analysed using Gwyddion software.

## 4.7 | Raman Spectroscopy

A Renishaw in Via Raman microscope was used to collect Raman spectra, with a 50x objective in a backscattering configuration. Spectra were collected using a 488 nm and 514 nm argon-ion laser and a 785 nm diode laser with laser power, acquisition time and defocus optimised to enable the best spectra and minimum laser degradation. Calibration of the filter and grating was performed using the well-defined  $520 \text{ cm}^{-1}$  peaks of a Si reference. For in situ Field Dependent Raman Spectroscopy (EFDRS), the same Raman protocols were used. The sample was contained in a Linkam HFS600E-PB4 sample chamber, and a drain voltage was applied across the source-drain electrodes. A constant  $V_D$  was applied and held for 2 min before Raman measurements were taken; 20 positions down the  $5 \mu\text{m}$  channel were probed at each applied voltage.

---

## Acknowledgements

The authors acknowledge the UK EPSRC for the Processable Electronics Centre for Doctoral Training (EP/L016702/1) funding and Application Targeted and Integrated Photovoltaics (ATIP) Programme Grant (EP/T028513/1) and National Research Foundation of Korea (NRF) grant

funded by the Ministry of Education (No. RS–2023–00301974). JSK thanks the Ewha Global Excellence Program.

## Funding

UKRI EPSRC Centre for Doctoral Training in Plastic Electronic Materials (EP/L016702/1) and EPSRC Programme Grant ATIP (Application Targeted and Integrated Photovoltaics) (EP/T028513/1).

## Conflicts of Interest

The authors declare no conflicts of interest.

## Data Availability Statement

The data that support the findings of this study are available from the corresponding author upon reasonable request.

## References

1. J. Kosco, S. Gonzalez-Carrero, C. T. Howells, et al., “Oligoethylene Glycol Side Chains Increase Charge Generation in Organic Semiconductor Nanoparticles for Enhanced Photocatalytic Hydrogen Evolution,” *Advanced Materials* 34 (2022): 2105007.
2. C. B. Nielsen, A. Giovannitti, D.-T. Sbircea, et al., “Molecular Design of Semiconducting Polymers for High-Performance Organic Electrochemical Transistors,” *Journal of the American Chemical Society* 138 (2016): 10252–10259.
3. E. Tan, J. Kim, K. Stewart, et al., “The Role of Long-Alkyl-Group Spacers in Glycolated Copolymers for High-Performance Organic Electrochemical Transistors,” *Advanced Materials* 34 (2022): 2202574.
4. S. E. Chen, L. Q. Flagg, J. W. Onorato, et al., “Impact of Varying Side Chain Structure on Organic Electrochemical Transistor Performance: A Series of Oligoethylene Glycol-Substituted Polythiophenes,” *Journal of Materials Chemistry A* 10 (2022): 10738–10749.
5. S. Torabi, F. Jahani, I. Van Severen, et al., “Strategy for Enhancing the Dielectric Constant of Organic Semiconductors Without Sacrificing Charge Carrier Mobility and Solubility,” *Advanced Functional Materials* 25 (2015): 150–157.
6. A. A. Mohapatra, Y. Dong, P. Boregowda, et al., “Rational Design of Donor–Acceptor Based Semiconducting Copolymers With High Dielectric Constants,” *The Journal of Physical Chemistry C* 125 (2021): 6886–6896.
7. A. Giovannitti, I. P. Maria, D. Hanifi, et al., “The Role of the Side Chain on the Performance of N-type Conjugated Polymers in Aqueous Electrolytes,” *Chemistry of Materials* 30 (2018): 2945–2953.
8. J. Brebels, J. V. Manca, L. Lutsen, D. Vanderzande, and W. Maes, “High Dielectric Constant Conjugated Materials for Organic Photovoltaics,” *Journal of Materials Chemistry A* 5 (2017): 24037–24050.
9. J. Liu, G. Ye, H. G. O. Potgieser, et al., “Amphiphathic Side Chain of a Conjugated Polymer Optimizes Dopant Location Toward Efficient N-Type Organic Thermoelectrics,” *Advanced Materials* 33 (2021): 2006694.
10. Y. He, N. A. Kukhta, A. Marks, and C. K. Luscombe, “The Effect of Side Chain Engineering on Conjugated Polymers in Organic Electrochemical Transistors for Bioelectronic Applications,” *Journal of Materials Chemistry C* 10 (2022): 2314–2332.
11. H. Yan, S. Limbu, X. Wang, et al., “Efficient Charge Carrier Injection and Balance Achieved by Low Electrochemical Doping in Solution-Processed Polymer Light-Emitting Diodes,” *Advanced Functional Materials* 29 (2019): 1904092.
12. C. M. Gordon, J. D. Holbrey, A. R. Kennedy, and K. R. Seddon, “Ionic Liquid Crystals: Hexafluorophosphate Salts,” *Journal of Materials Chemistry* 8 (1998): 2627–2636.
13. C. J. Bowlas, D. W. Bruce, and K. R. Seddon, “Liquid-Crystalline Ionic Liquids,” *Chemical Communications* 14 (1996): 1625–1626.
14. M. Zagórska, E. Taler, I. Kulszewicz-Bajer, A. Proń, and J. Nizioł, “Conductive Polyaniline-Polyamide 6 Blends Processed From Formic Acid with Improved Stability Against Deprotonation,” *Journal of Applied Polymer Science* 73 (1999): 1423–1426.
15. K. Choi, S. Im, A. Plant, et al., “Role of Amorphous Phases in Mixed Conduction of Conjugated Regioblock Copolymers for Organic Electrochemical Synaptic Transistors,” *Advanced Materials* 37 (2025): 21133.
16. S. Limbu, K. Stewart, J. Nightingale, et al., “Solid-State Ionic Liquid: Key to Efficient Detection and Discrimination in Organic Semiconductor Gas Sensors,” *ACS Applied Electronic Materials* 3 (2021): 2152–2163.
17. K. Stewart, K. Pagano, E. Tan, et al., “Understanding Effects of Alkyl Side-Chain Density on Polaron Formation Via Electrochemical Doping in Thiophene Polymers,” *Advanced Materials* 36 (2024): 221184.
18. H. Hu, K. Zhao, N. Fernandes, et al., “Entanglements in Marginal Solutions: A Means of Tuning Pre-Aggregation of Conjugated Polymers with Positive Implications for Charge Transport,” *Journal of Materials Chemistry C* 3 (2015): 7394–7404.
19. Z. Xue, D. He, and X. Xie, “Poly(Ethylene Oxide)-Based Electrolytes for Lithium-Ion Batteries,” *Journal of Materials Chemistry A* 3 (2015): 19218–19253.
20. H. J. Cheon, T. K. An, and Y.-H. Kim, “Diketopyrrolopyrrole (DPP)-Based Polymers and Their Organic Field-Effect Transistor Applications: A Review,” *Macromolecular Research* 30 (2022): 71–84.
21. R. Di Pietro, T. Erdmann, J. H. Carpenter, et al., “Synthesis of High-Crystallinity DPP Polymers with Balanced Electron and Hole Mobility,” *Chemistry of Materials* 29 (2017): 10220–10232.
22. I. Kang, H.-J. Yun, D. Sung Chung, S.-K. Kwon, and Y.-H. Kim, “Record High Hole Mobility in Polymer Semiconductors via Side-Chain Engineering,” *Journal of the American Chemical Society* 135 (2013): 14896.
23. H. Huang, Z. Chen, R. P. Ortiz, et al., “Combining Electron-Neutral Building Blocks With Intramolecular “Conformational Locks” Affords Stable, High-Mobility P- and N-Channel Polymer Semiconductors,” *Journal of the American Chemical Society* 134 (2012): 10966–10973.
24. H. Yu, K. H. Park, I. Song, M.-J. Kim, Y.-H. Kim, and J. H. Oh, “Effect of the Alkyl Spacer Length on the Electrical Performance of Diketopyrrolopyrrole-Thiophene Vinylene Thiophene Polymer Semiconductors,” *Journal of Materials Chemistry C* 3 (2015): 11697–11704.
25. M. J. Cho, J. Shin, T. R. Hong, et al., “Diketopyrrolopyrrole-Based Copolymers Bearing Highly  $\pi$ -Extended Donating Units and Their Thin-Film Transistors and Photovoltaic Cells,” *Polymer Chemistry* 6 (2015): 150–159.
26. W. Cui and F. Wudl, “Dithienylbenzodipyrrolidone: New Acceptor for Donor–Acceptor Low Band Gap Polymers,” *Macromolecules* 2013, 46, 7232–7238.
27. T. J. Aubry, K. J. Winchell, C. Z. Salamat, et al., “Tunable Dopants with Intrinsic Counterion Separation Reveal the Effects of Electron Affinity on Dopant Intercalation and Free Carrier Production in Sequentially Doped Conjugated Polymer Films,” *Advanced Functional Materials* 30 (2020): 2001800.
28. S. H. Yu, K. H. Park, Y.-H. Kim, D. S. Chung, and S.-K. Kwon, “Fine Molecular Tuning of Diketopyrrolopyrrole-Based Polymer Semiconductors for Efficient Charge Transport: Effects of Intramolecular Conjugation Structure,” *Macromolecules* 50 (2017): 4227–4234.
29. S. Wood, J. Wade, M. Shahid, et al., “Natures of Optical Absorption Transitions and Excitation Energy Dependent Photostability of Diketopyrrolopyrrole (DPP)-Based Photovoltaic copolymers,” *Energy & Environmental Science* 8 (2015): 3222–3232.
30. M. Rejsjalali, J. J. Burgos-Mármol, R. Manurung, and A. Troisi, “Local Structuring of Diketopyrrolopyrrole (DPP)-Based Oligomers from Molecular Dynamics Simulations,” *Physical Chemistry Chemical Physics* 23 (2021): 19693–19707.

31. M. Moser, A. Savva, K. Thorley, et al., "Polaron Delocalization in Donor-Acceptor Polymers and its Impact on Organic Electrochemical Transistor Performance," *Angewandte Chemie International Edition* 60 (2021): 7777–7785.
32. Y. Ding, Y. Zhu, H. Wang, et al., "Improving Electrical and Mechanical Properties of Blend Films via Optimizing Solution-Processable Techniques and Controlling the Semiconductor Molecular Weight," *Macromolecules* 55 (2022): 8577–8589.
33. K. Stewart, S. Limbu, J. Nightingale, et al., "Molecular Understanding of a  $\pi$ -Conjugated Polymer/Solid-State Ionic Liquid Complex as a Highly Sensitive and Selective Gas Sensor," *Journal of Materials Chemistry C* 8 (2020): 15268–15276.
34. A. N. Mallya, R. Kottokkaran, and P. C. Ramamurthy, "Conducting Polymer–Carbon Black Nanocomposite Sensor for Volatile Organic Compounds and Correlating Sensor Response by Molecular Dynamics," *Sensors and Actuators B: Chemical* 201 (2014): 308–320.
35. L. Kergoat, B. Piro, M. Berggren, G. Horowitz, and M.-C. Pham, "Advances in Organic Transistor-Based Biosensors: From Organic Electrochemical Transistors to Electrolyte-Gated Organic Field-Effect Transistors," *Analytical and Bioanalytical Chemistry* 402 (2012): 1813–1826.
36. S. Kwon, Y. Pak, B. Kim, et al., "Molecular-Level Electrochemical Doping for Fine Discrimination of Volatile Organic Compounds in Organic Chemiresistors," *Journal of Materials Chemistry A* 8 (2020): 16884–16891.
37. A. Kokil, K. Yang, and J. Kumar, "Techniques for Characterization of Charge Carrier Mobility in Organic Semiconductors," *Journal of Polymer Science Part B: Polymer Physics* 50 (2012): 1130–1144.
38. L. Ma, W. H. Lee, Y. D. Park, J. S. Kim, H. S. Lee, and K. Cho, "High Performance Polythiophene Thin-Film Transistors Doped with Very Small Amounts of an Electron Acceptor," *Applied Physics Letters* 92 (2008): 063310.
39. C. Liu, J. Jang, Y. Xu, et al., "Effect of Doping Concentration on Microstructure of Conjugated Polymers and Characteristics in N-Type Polymer Field-Effect Transistors," *Advanced Functional Materials* 25 (2015): 758–767.
40. J. Yin, Z. Wang, D. Fazzi, Z. Shen, and C. Soci, "First-Principles Study of the Nuclear Dynamics of Doped Conjugated Polymers," *The Journal of Physical Chemistry C* 120 (2016): 1994–2001.
41. A. A. Virkar, S. Mannsfeld, Z. Bao, and N. Stingelin, "Organic Semiconductor Growth and Morphology Considerations for Organic Thin-Film Transistors," *Advanced Materials* 22 (2010): 3857–3875.
42. A. Dodabalapur, L. Torsi, and H. E. Katz, "Organic Transistors: Two-Dimensional Transport and Improved Electrical Characteristics," *Science* 268 (1995): 270–271.
43. J. L. Brédas, D. Beljonne, V. Coropceanu, and J. Cornil, "Charge-Transfer and Energy-Transfer Processes in  $\pi$ -Conjugated Oligomers and Polymers: a Molecular Picture," *Chemical Reviews* 104 (2004): 4971.
44. S. R. Marder, C. B. Gorman, B. G. Tiemann, J. W. Perry, G. Bourhill, and K. Mansour, "Relation Between Bond-Length Alternation and Second Electronic Hyperpolarizability of Conjugated Organic Molecules," *Science* 261 (1993): 186–189.
45. Z. Yu, Y. Lu, J. Wang, and J. Pei, "Conformation Control of Conjugated Polymers," *Chemistry—A European Journal* 26 (2020): 16194–16205.
46. D. G. Seo, G. T. Go, H. L. Park, and T. W. Lee, "Organic Synaptic Transistors for Flexible and Stretchable Artificial Sensory Nerves," *MRS Bulletin* 46 (2021): 321–329.
47. N. Kim, G.-T. Go, H.-L. Park, et al., "Molecular Tailoring to Achieve Long-Term Plasticity in Organic Synaptic Transistors for Neuromorphic Computing," *Advanced Intelligent Systems* 5 (2023): 2300016.
48. H. Tang, Z. Qin, J. Jiang, et al., "Tailoring Side Chain in Organic Donor-Pi-Acceptor Copolymeric Mixed Conductors for Efficient and Extremely Stable Artificial Synapses," *Small* 21 (2025): 05310.
49. T. Park, M. Kim, E. K. Lee, J. Hur, and H. Yoo, "Overcoming Downscaling Limitations in Organic Semiconductors: Strategies and Progress," *Small* 20 (2024): 2306468.
50. G.-T. Go, Y. Lee, D.-G. Seo, et al., "Achieving Microstructure-Controlled Synaptic Plasticity and Long-Term Retention in Ion-Gel-Gated Organic Synaptic Transistors," *Advanced Intelligent Systems* 2 (2020): 2000012.
51. Y. Shi, J. Liu, Y. Hu, W. Hu, and L. Jiang, "Effect of Contact Resistance in Organic Field-Effect Transistors," *Nano Select* 2 (2021): 1661–1681.
52. M. J. Frisch, G. W. Trucks, H. B. Schlegel, et al., Gaussian 09 (Gaussian, Inc., Wallingford CT, 2009).
53. A. D. Becke, "Density-Functional Thermochemistry. III. The Role of Exact Exchange," *The Journal of Chemical Physics* 98 (1993): 5648–5652.
54. G. A. Petersson, A. Bennett, T. G. Tensfeldt, M. A. Al-Laham, W. A. Shirley, and J. Mantzaris, "A Complete Basis Set Model Chemistry. I. The Total Energies of Closed-Shell Atoms and Hydrides of the First-Row Elements," *The Journal of Chemical Physics* 89 (1988): 2193–2218.
55. P. J. Stephens, F. J. Devlin, C. F. Chabalowski, and M. J. Frisch, "Ab Initio Calculation of Vibrational Absorption and Circular Dichroism Spectra Using Density Functional Force Fields," *The Journal of Physical Chemistry* 98 (1994): 11623–11627.
56. M. L. Laury, M. J. Carlson, and A. K. Wilson, "Vibrational Frequency Scale Factors for Density Functional Theory and the Polarization Consistent Basis Sets," *Journal of Computational Chemistry* 33 (2012): 2380–2387.
57. R. Dennington, T. A. Keith, and J. M. Millam GaussView, Version 6.0, (Semicem Inc, Shawnee Mission, KS, 2016).

### Supporting Information

Additional supporting information can be found online in the Supporting Information section.

**Supporting File:** aelm70307-sup-0001-SuppMat.docx.